AIAA Aviation
22-26 June 2015, Dallas, TX
22nd AIAA Computational Fluid Dynamics Conference

Extension of the SU2 Open Source CFD code to the simulation of turbulent flows of fluids modelled with complex thermophysical laws

Salvatore Vitale* Giulio Gori† Thomas D. Economon‡
Matteo Pini* Alberto A. Guardone† Francisco Palacios§
Piero Colonna* Juan J. Alonso‡

This paper presents the extension of the open source SU2 software suite to perform turbulent Non-Ideal Compressible Fluid-Dynamics (NICFD) simulations. A new built-in thermodynamic library has been developed and tightly coupled with the existing structure of the code, properly re-organized for accommodating arbitrary thermophysical models. The library implements simple models and interfaces to an external software for a more accurate estimation of thermophysical properties of NICFD pure fluids and mixtures. Moreover, the Reynolds-averaged Navier-Stokes (RANS) equations are spatially discretized by resorting to suitably defined convective and viscous numerical schemes for general fluids.
The capabilities of the code are finally verified on two- and three-dimensional inviscid and turbulent flow problems against solutions obtained with different NICFD solvers, and known analytical ones. The results prove that SU2 is comparatively accurate and computational efficient with respect to existing codes. Definitively, SU2 can be considered as a trustworthy tool for NICFD-based simulations and the future pillar of advanced automated design techniques involving complex fluid laws.

Introduction

SU2 software suite[1] has recently became a well-established open-source platform for solving multi-physics PDE problems and PDE-constrained optimization problems on general unstructured meshes. The core of the suite is a Reynolds-averaged Navier-Stokes (RANS) solver capable of simulating the compressible, turbulent flows typical of aerospace engineering problems. SU2 was constructed with aerodynamic shape optimization problems in mind, and, therefore, adjoint-based sensitivity analysis is a key feature of the RANS package.
As common practice in the aerodynamic field, SU2 thermodynamic capability is restricted only to fluids obeying the perfect gas law, i.e. the medium is supposed to behave as a dilute gas with no molecular interactions. Though perfect gas approximation is usually realistic for a variety of aerospace and turbomachinery flow problems, it is profoundly questionable when dealing with compounds characterized by attractive and repulsive forces at the molecular scale. For the sake of simplicity, fluid flows departing from ideality are globally referred to as Non-Ideal Compressible Fluid flows.
More precisely, we mean with Non-Ideal Compressible Fluid-Dynamics (NICFD) the branch of fluid-mechanics studying the actual characteristics of dense vapors, supercritical flows and compressible two-phase flows, namely whereby the thermodynamic behavior of the fluid differs considerably from that of a perfect gas. At high reduced pressure and temperature, close to the saturation curve the speed of sound is largely sensitive to density variations along isentropes. Consequently, the fluid flow departs from the ideality assumption and under particular conditions may even exhibit non-classical gas-dynamic phenomena, whose nature is governed by the value of the fundamental derivative of gas-dynamics Γ.[2] A non-monotonic Mach number trend along expansion is typical for $0 < \Gamma < 1$, while negative $\Gamma < 0$ values admit the occurrence of inverse

*Propulsion and Power, Delft University of Technology, The Netherlands
†CREA Laboratory, Politecnico di Milano, Italy
‡Aerospace Design Laboratory, Stanford University, United States.
§The Boeing Company, Everett, United States.

gas-dynamics phenomena such as rarefaction shock waves, splitting waves or even composite waves. Inverse gas-dynamics behavior has been theoretically predicted for heavy complex molecules[3] in the vapor region, and a recent study discovered that two-phase rarefaction shock waves are physically realizable close to the critical point of simple compounds.[4]

Applications of NICFD flows to industrial problems are already numerous and spread over heterogeneous fields. Basically, they are encountered in Organic Rankine Cycle (ORC) turbogenerators, which are energy conversion systems renowned for the efficient exploitation of renewable power sources.[5–8] Refrigeration industry is looking at novel solutions using supercritical CO_2 streams in compressors ($scCO_2$); a number of research projects are actively ongoing for defining implications in terms of turbomachinery design .[9,10] Supercritical CO_2 power cycles represent a valuable alternative for next generation nuclear reactors.[11] NICFD flows frequently occur in pharmaceutical processing,[12] transportation of fuels at high-speed,[13] and in transonic and supersonic wind tunnels.[14] Furthermore, the increasingly stringent environmental regulation in the aerospace sector is pushing the attention towards green technologies for next generation aircrafts, such as unconventional compact on-board energy systems for optimal thermal management. Ultimately, all these kinds of systems which NICFD fluids as energetic carrier.

The performance of the aforementioned technologies would definitely gain from a thorough understanding of the complex physics of various NICFD phenomena. Reliable simulations of such flows still represents a research task, as it necessitates sophisticated tools coupled with highly complex and experimentally calibrated thermodynamic models. The joint research team formed by Delft University of Technology, Politecnico di Milano, and Stanford University is undertaking a collaborative effort to i) bring the SU2 to the cutting-edge for NICFD simulations ii) validate the code against experiments that are currently underway at the first two institutions iii) achieve a highly automated design framework for innovative system concepts dealing with these fluids. The (SU2) suite already incorporates a library for thermophysical properties of reacting non-equilibrium flows, though a computational framework for NICFD simulations is still completely missing. Hence, this work is the early step to fill this gap by extending the compressible infrastructure to treat non-ideal compressible fluid flows. All the modifications are released in compliance with the open-source philosophy of the project, thus contributing to promote a worldwide access to state-of-the-art analysis tools. The implementation leverages on the vast knowledge acquired by the authors with past studies on dense-gas flows and previous experience on dense-gas CFD solvers.[15–19] In line with the programming paradigm of (SU2), a high level of abstraction and modularity is pursued, with the aim of easing the implementation of further features within the new release. More specifically, a new built-in thermodynamic library has been developed and tightly coupled with the existing structure of the code, properly re-organized for accommodating arbitrary thermophysical models. The library includes the polytropic ideal gas (PIG), the polytropic Van der Waals (PVdW), and the polytropic Peng-Robinson (PR) models. Moreover, the library interfaces to a a more accurate external software[20] for the estimation of thermophysical properties of pure fluids and mixtures. Concerning numerical methods, the inviscid fluxes and Jacobian contribution are generalized following the Vinokur-Montagnè approximate Riemann solver (ARS)[21,22] while the Averaged-Gradient (AVG) formulation is used for the viscous counterpart.

The new solver is capable of solving the fully compressible turbulent Navier-Stokes equations with arbitrarily complex equations of state in two and three dimensions using the Spalart-Allamaras (SA) and the Menter Shear-Stress-Tensor kω-SST turbulence models. In the end, the code is built to be a versatile platform for simulating the flow physics of dense vapors of pure fluids, mixtures and two-phase flows at equilibrium conditions with explicit and implicit time-marching schemes.

The paper is organized as follows: section I recalls the governing equations for an arbitrarily complex fluid at equilibrium condition. Section II describes the chosen numerical methods, with particular emphasis on convective, viscous and boundary conditions schemes. Section III briefly outlines the thermophysical models currently available in SU2, while section IV concludes the paper by illustrating an ensemble of test cases for verification purpose.

I. Generalized Flow Equations

The present work focuses on the compressible formulation of the Reynolds-Averaged Navier-Stokes (RANS) equations,[23] as high Mach number flows are of predominant interest. Compressible RANS equations are usually discretized by resorting to a suitably defined conservative formulation. The system of PDE equations including the inviscid and viscous terms is written as

$$\partial_t U + \nabla \cdot \vec{F}^c - \nabla \cdot \vec{F}^v = Q \quad \text{in } \Omega,\ t > 0. \tag{1}$$

Equation (1) describes how mass, momentum and energy evolve in a control domain. $\vec{U}$ symbolizes the vector of conservative variables, i.e. $\vec{U} = (\rho, \rho v_1, \rho v_2, \rho v_3, \rho E)^\intercal$, where ρ is the fluid density, E is the total energy per unit mass, and $\vec{v} = (v_1, v_2, v_3) \in \mathbb{R}^3$ is the flow velocity in a Cartesian coordinate system. In this particular model, convective and viscous fluxes are given by

$$\vec{F}_i^c = \begin{pmatrix} \rho v_i \\ \rho v_i v_1 + P\delta_{i1} \\ \rho v_i v_2 + P\delta_{i2} \\ \rho v_i v_3 + P\delta_{i3} \\ \rho v_i H \end{pmatrix}, \quad \vec{F}_i^v = \begin{pmatrix} \cdot \\ \tau_{i1} \\ \tau_{i2} \\ \tau_{i3} \\ v_j \tau_{ij} + k_{\text{tot}} \partial_i T \end{pmatrix}, \quad i = 1, \ldots, 3. \tag{2}$$

P is the static pressure, T is the temperature, H is the total enthalpy, δ_{ij} is the Kronecker delta function, and the viscous stresses can be compactly written as $\tau_{ij} = \mu_{tot}\left(\partial_j v_i + \partial_i v_j - \frac{2}{3}\delta_{ij}\nabla \cdot \vec{v}\right)$. Recall that latin indices i, j denote 3-D Cartesian coordinates with repeated indices implying summation.
According to the Boussinesq hypothesis,[24] μ_{tot} and k_{tot} are respectively the total viscosity and the total thermal conductivity, resulting from a molecular, μ_{mol},k_{mol} and a turbulent, μ_{tur}, k_{tur} contribution (3). The molecular quantities are evaluated by means of transport property models, μ_{tur} is given by turbulence model, whereas k_{tur} is simply a linear combination of the turbulent Prandtl number Pr_t, the specific heat capacity at constant pressure C_p, and μ_{tur} (4). For further details about turbulence closures in SU2 refer to previous papers.[1]

$$\mu_{\text{tot}} = \mu_{\text{mol}} + \mu_{\text{tur}}, \quad k_{\text{tot}} = k_{\text{mol}} + k_{\text{tur}}, \tag{3}$$

$$k_{\text{tur}} = \frac{C_p \mu_{\text{tur}}}{Pr_t}. \tag{4}$$

To close (1), the system of equations is supplemented by constitutive relations. By limiting the analysis to newtonian fluids and Fourier's law, a fluid model and a turbulence closure are needed to evaluate the quantities $P, T, C_p, \mu_{\text{mol}}, k_{\text{mol}}, \mu_{\text{tur}}$. In case of pure fluids or mixture of given composition, the thermodynamic state is completely defined by two independent quantities, reasonably being density ρ and internal energy e in compressible CFD codes; their dependency on the conservative vector can be written as

$$\rho = U_1, \quad e = \frac{U_5}{U_1} - \frac{(U_2 + U_3 + U_4)^2}{2U_1^2} = E - \frac{\|v\|^2}{2}, \tag{5}$$

and P, T are determined using the thermodynamic model as

$$P = P(\rho, e) = P(U), \quad T = T(\rho, e) = T(U), \tag{6}$$

Specific heat capacity C_p and transport quantities are conveniently expressed as

$$\begin{aligned} \mu_{\text{mol}} &= \mu_{\text{mol}}(\rho, T) = \mu_{\text{mol}}(\rho, T(\rho, e)) = \mu_{\text{mol}}(U), \\ k_{\text{mol}} &= k_{\text{mol}}(\rho, T) = k_{\text{mol}}(\rho, T(\rho, e)) = k_{\text{mol}}(U), \\ C_p &= C_p(P, T) = C_p(P(\rho, e), T(\rho, e)) = C_p(U). \end{aligned} \tag{7}$$

The code structure has been re-adapted to compute these thermodynamic quantities potentially using any desired thermophysical model, and those currently available on SU2 are recalled in Section III.

II. Numerical Algorithms

This section schematically explains the numerical methods adopted for solving the compressible PDE with arbitrary fluid model. Particular emphasis is put on the spatial discretization schemes, with focus on the generalized Roe's ARS to evaluate convective fluxes and the AVG formulation for viscous fluxes.

A. Space integration

SU2 has a standard edge-based structure on a dual grid with control volumes constructed using a median-dual vertex-based scheme as shown in Fig. 1. Equation 8 shows the semi-discretized integral form of PDE:

$$\int_{\Omega_i} \frac{\partial U}{\partial t}\, d\Omega + \sum_{j \in \mathcal{N}(i)} (\tilde{F}_{c_{ij}} + \tilde{F}_{v_{ij}}) \Delta S_{ij} - Q|\Omega_i| = \int_{\Omega_i} \frac{\partial U}{\partial t}\, d\Omega + R_i(U) = 0, \tag{8}$$

where $R_i(U)$ is the residual. $\tilde{F}_{c_{ij}}$ and $\tilde{F}_{v_{ij}}$ are the projected numerical approximations of the convective and viscous fluxes, respectively, ΔS_{ij} is the area of the face associated with the edge ij, Ω_i is the volume of the control volume and $\mathcal{N}(i)$ are the neighboring nodes to node i.

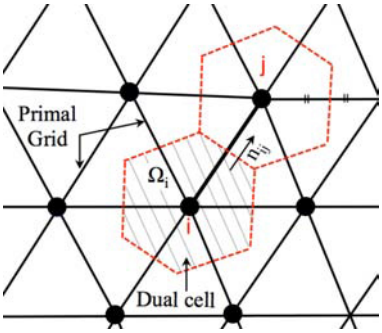

Figure 1. Schematic of the primal mesh and the control volume on a dual mesh.

The convective and viscous fluxes are evaluated at the midpoint of an edge. The numerical solver loops through all of the edges in the primal mesh in order to calculate these fluxes and then integrates them to evaluate the residual at every node in the numerical grid.

B. Convective fluxes

Several ARSs have been recently generalized without assuming a specific thermodynamic model.[17] However, at moment, there is no particular evidence of the superiority of one formulation compared the others. In the present work we consequently decided to start implementing the popular Roe's scheme with the plan of enriching the convective flux library of additional schemes (e.g. AUSM+, HLLC, centered-type) in a subsequent release. The convective fluxes are then reconstructed from flow quantities separately on both sides of the face of the control volume retrieving the values at the surrounding nodes:

$$\tilde{F}_{c_{\mathrm{ij}}} = \tilde{F}(U_{\mathrm{i}}, U_{\mathrm{j}}) = \left(\frac{\vec{F}^c_{\mathrm{i}} + \vec{F}^c_{\mathrm{j}}}{2} \right) \cdot \vec{n}_{\mathrm{ij}} - \frac{1}{2} P|\Lambda|P^{-1}(U_i - U_j), \tag{9}$$

where $\vec{n}_{ij}$ is the outward unit normal associated with the face between nodes i and j, U_i is the vector of the conserved variables at point i and $\vec{F}^c_i$ is the convective physical flux at node i. P and P^{-1} are respectively the right and the left eigenvectors of the Jacobian of the physical flux with respect to the conservative variables, constructed using the Roe averaged variables and projected in the $\vec{n}_{ij}$ direction, and $|\Lambda|$ is a diagonal matrix with entries corresponding to the absolute value of the eigenvalues of the same Jacobian.

The generalization of (9) practically reduces to apply the general fluid model assumption to the spectral decomposition of the Roe's averaged state Jacobian, i.e. to the eigenstructure of $P|\Lambda|P^{-1}$, see VI for more details. Contrary to the ideal gas formulation, from the Roe averaging procedure (10) a supplemental condition arises (11), namely:

$$\left(\vec{F}^c_{\mathrm{i}} - \vec{F}^c_j \right) = \bar{A}\left(U_{\mathrm{i}} - U\mathrm{j} \right), \quad \bar{A} = A(\bar{U}), \tag{10}$$

$$\bar{\chi}(\rho_{\mathrm{i}} - \rho_{\mathrm{j}}) + \bar{\kappa}(\rho_{\mathrm{i}} e_{\mathrm{i}} - \rho_{\mathrm{i}} e_{\mathrm{j}}) = (P_{\mathrm{i}} - P_{\mathrm{j}}), \tag{11}$$

where $\bar{\chi}$ and $\bar{\kappa}$ are the average of these two thermodynamics quantities defined in (12)

$$\chi = \left(\frac{\partial P}{\partial \rho}\right)_{\rho e} = \left(\frac{\partial P}{\partial \rho}\right)_{e} - \frac{e}{\rho}\left(\frac{\partial P}{\partial e}\right)_{\rho} \qquad , \kappa = \left(\frac{\partial P}{\partial \rho e}\right)_{\rho} = \frac{1}{\rho}\left(\frac{\partial P}{\partial e}\right)_{\rho}. \tag{12}$$

For a fluid obeying the PIG law χ is equal to zero and κ is a constant equal to $\gamma - 1$. Therefore, condition (11) is identically satisfied for all intermediate state. On the other hand, if a not-ideal model is used, only one relation (11) is provided for the two unknowns $\bar{\chi}$ and $\bar{\kappa}$. Consequently, the Roe-average state remains uniquely defined if and only if a proper closure condition is given. Several approaches[22,25–27] have been proposed in the past to close such problem and the one suggested by Vinokur-Montagne'[22] is implemented in SU2.
Second-order accuracy is resolved using a Monotone Upstream-centered Schemes for Conservation Laws (MUSCL) approach[28] with gradient limitation.

C. Viscous fluxes

The numerical viscous flux is evaluated by averaging the flow variables, flow derivatives, and transport properties at two neighboring cells, (13) and (14).

$$x_{\mathrm{m}} = \frac{x_{\mathrm{i}} + x_{\mathrm{j}}}{2}, \tag{13}$$

$$\tilde{F}_{v_{\mathrm{ij}}} = \vec{F}^{v}(v_{\mathrm{m}}, \partial_{\mathrm{m}}, \mu_{\mathrm{m}}, k_{\mathrm{m}}, ...). \tag{14}$$

While previous works followed the approach of Pulliam and Steger[29] for obtaining diffusive flux Jacobian, a formulation based on the conservative variables is considered in SU2. To simplify the derivation, *Thin Shear-Layer* approximation[30] is employed for gradient calculation.

D. Riemann Boundary Conditions

The imposition of suitable boundary conditions at the so-called free boundaries is discussed here. The number of physical variables that can be imposed freely at a boundary is dependent on the propagation properties of the system. Each wave (characteristic variable) transports a given information, and also the quantities transported from the inside of the domain towards the boundary will influence and modify the situation along the boundary. Hence, only variables transported from the boundaries towards the interior can be freely imposed at the boundaries, while the remaining variables depend on the computed flow interior solution. To this purpose, a new type of boundary condition, named Riemann, has been added to the SU2 suite, which implements the approach proposed in[31] to automatically detect inflow/outflow boundaries for hyperbolic systems. By means of an eigenvalue analysis the right number of enforceable unknowns is determined, and the variables that can be specified at the boundary are automatically selected.
Considering a system of non-linear hyperbolic equations, such as the Euler equations for compressible flows

$$\partial_t \vec{U} + \nabla \vec{F}\left(\vec{U}\right) = 0. \tag{15}$$

The system (15) is linearized along the outward normal direction $\vec{n}$ as follows

$$\partial_t \vec{U} + A\,\partial_{\vec{n}} \vec{U} = 0, \tag{16}$$

where $A = \partial_{\vec{U}} \vec{F}(\vec{U}) \cdot \vec{n} = P \Lambda P^{-1}$, with $\partial_{\vec{n}}$ derivative along $\vec{n}$. Matrix A, P and Λ are evaluated locally at the each boundary node. The required boundary value can be established by analyzing the sign of the eigenvalues of matrix A. Equation 17 introduces the characteristic variables jump

$$\delta \vec{v} \equiv P^{-1} \delta \vec{U} = P^{-1}\left(\vec{U}_e - \vec{U}_i\right), \tag{17}$$

where the quantity $\delta \vec{U} = \vec{U}_e - \vec{U}_i$ is the difference between the outer conservative vector $\vec{U}_e$ and the solution $\vec{U}_i$ at the i-th boundary node. A characteristic line entering the domain is related to a locally negative eigenvalue, this means that the information carried by the characteristic line travels across the boundary inside the domain. Therefore, in case of a negative eigenvalue, the boundary value will be imposed by the corresponding component of the vector $\vec{U}_e$. Otherwise, if the eigenvalue is non-negative, the values at

the boundary are specified by means of the values taken from the internal solution $\vec{U}_i$. Re-defining the characteristic jump as

$$\delta\bar{v}_i = \begin{cases} \delta v_i^{ext} & \text{if } \lambda < 0 \\ 0 & \text{if } \lambda \geq 0 \end{cases} \tag{18}$$

and the new operator $\psi(\lambda)$

$$\psi_i = \psi(\lambda_i) = \begin{cases} 1 & \text{if } \lambda_i < 0 \\ 0 & \text{if } \lambda_i \geq 0 \end{cases} \tag{19}$$

we obtain

$$\delta\bar{v}_i = \psi_i \left(P^{-1} \left[\vec{U}_e - \vec{U}_i \right] \right). \tag{20}$$

The boundary value of the unknown therefore reads

$$\vec{U}_b = \vec{U}_i + P\,\mathrm{diag}(\vec{\psi})\,P^{-1} \left[\vec{U}_e - \vec{U}_i \right], \tag{21}$$

which is used to compute the numerical fluxes at the boundary.
This particular approach is very useful whenever the inflow and the outflow boundary cannot be identified properly, this is typical of simulation involving circular domain (like a pitching airfoil in a free-stream field), in non-physical initialization of the solution for steady problems and in all situations where the boundary type (inflow/outflow) changes during the simulations.

III. Thermophysical library

The new SU2 thermophysical library has been devised with a high-level of object orientation and abstraction in mind, meaning that the code can be easily inspected and further enriched by other developers. From classical thermodynamics, the state of the fluid is univocally determined by means of a volumetric, i.e. $P = P(T, v)$, and a caloric, i.e. $e = e(T, v)$, equation of state. Alternatively, the state can be completely specified by a means of a fundamental relation $\Phi = \Phi(T, v)$, Φ being a thermodynamic potential (e.g. Helmholtz, Gibbs). For instance, complex multi-parameter models, which accurately describe the flow characteristics of polar and non-polar heavy molecules in the single-phase dense gas region, originates from this second approach.
In order to create a flexible and re-usable thermodynamic infrastructure, we established built-in functions for simple volumetric and caloric EoS, while leaving the property calculation with comparatively high-fidelity models to external tools. Precisely, the library currently supports three built-in models, i.e. the polytropic ideal gas (PIG), the polytropic Van der Waals (PVdW), and the polytropic Peng-Robinson (PR) models. The interested reader can refer to VI for full description of the equations. As in the ideal gas version, transport properties are defined through the Sutherland's law and a constant Prandtl number.
Furthermore, the code is interfaced to an external and general purpose thermophysical library[20] originating at Delft University of Technology. The latter is under continuous development with regular improvements on equation accuracy in the critical region of fluids and introduction of new models. Noteworthy, it contains several thermophysical models and provides easy access to quantities necessary for SU2 simulation, with possibility of switching to Look-up Table (LuT) approach for faster computations.[17,32]

IV. Verification

The validation process of CFD tools is definitely an essential requirement to severely assess the accuracy of the results and to verify the reliability of the numerical methods considered. Although many experimental data are available for standard aerodynamic applications, very few experiments on NICFD flows have been performed so far. For the flow problems under scrutiny here no experimental data are publicly available, thus not permitting an actual validation campaign of the code. Therefore, this section presents only a comprehensive verification of SU2 against numerical solutions obtained with other NICFD solvers or known analytical solutions for different inviscid and viscous flow problems.

A. 2D inviscid supersonic nozzle

The first application is the 2D simulation of inviscid quasi-uniform supersonic flow in a converging-diverging nozzle. The selected fluid is siloxane MDM, modeled by means of the polytropic Van der Waals model. The SU2 prediction is compared against the results obtained through the zFlow solver,[15] a hybrid finite-volume/finite-element inviscid flow code specifically developed for fundamental studies on dense gas-dynamics of complex fluids using unstructured grids. zFlow features are somewhat similar to the ones of SU2, allowing for quick and reliable comparison for frictionless simulations. The calculation is performed on an unstructured grid composed by 12115 triangular elements. The main parameters of the simulation are summarized in Table 1.

The results of the two calculations are depicted in Figure 2 and 3. Figure 2 shows the streamwise Mach number distribution while Figure 3 confronts the Mach number evolution along the nozzle symmetry axis. Generally, the trend is well captured by SU2, though deviations are observed in the rear part of the diverging portion; seemingly, the zFlow computation is less diffusive in the high speed supersonic region. Such variation may be explained by the fact that the two codes adopt slightly different numerical algorithms, i.e SU2 and zFlow utilize diverse second-order spatial schemes (TVD against MUSCL) and boundary conditions approach. Nonetheless, it worth mentioning that no experimental validation was previously carried out on the zFlow code, therefore no superior accuracy may be claimed for this tool. As a consequence, the discrepancy between the two simulation are quantitatively acceptable for a first numerical verification of SU2.

Fluid	MDM
Thermodynamic model	PVdW
Gas Constant	35.23 J/K/kg
Specific heat ratio	1.12
Critical temperature	563.1 K
Critical pressure	14.15 bar
Total inlet temperature	543.0 K
Total inlet pressure	10.0 bar
Spatial scheme	Upwind generalized Roe 2^{nd} order

Table 1. Input data for the 2D supersonic nozzle simulation.

B. RANS simulation of a 2D cascade

The second test investigates the capability of SU2 in predicting turbulent flow through the VKI LS-89 turbine cascade. As in the previous test case, the working fluid is the siloxane MDM modeled now using the external library, more precisely the Span-Wagner model.[33] Approximately 16000 triangular elements are used to discretize the domain around the blade; no-slip condition is applied on the solid wall, and periodicity is set on the upper and the lower boundaries, while transport properties are kept constant at inlet condition. The remaining input parameters of the simulation are summarized in Table 2. SU2 results are herein confronted against the results provided by Joe,[34] a compressible Navier-Stokes solver recently extended to simulate NICFD flows and also coupled with same thermophysical library. The two platforms share most of the numerical features, thus enabling to prove the performance of SU2 against a tool of comparable accuracy. Figure 4 show the Mach flowfield; streamwise evolution of density, temperature, pressure, and Mach number along the cascade channel are reported in Fig. 5-8. The quantities are found to be in a very good accordance, demonstrating that SU2 turbulent features work correctly.

C. RANS simulation of a 3D nozzle with a wedge

SU2 capabilities are now investigated by simulating 3D turbulent flow in a converging-diverging nozzle with a sharp obstacle disturbing the core flow, see Fig. 9. The aim is to gain insight of the code performance when dealing with highly separated flow and shockwave-boundary layer interactions. No-slip boundary condition is applied on the upper, left, right and wedge surface, while symmetry condition is specified at bottom surface.

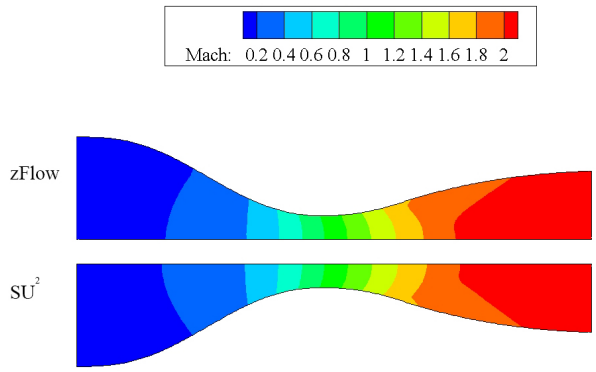

Figure 2. Mach contours of the 2D nozzle for both CFD solvers.

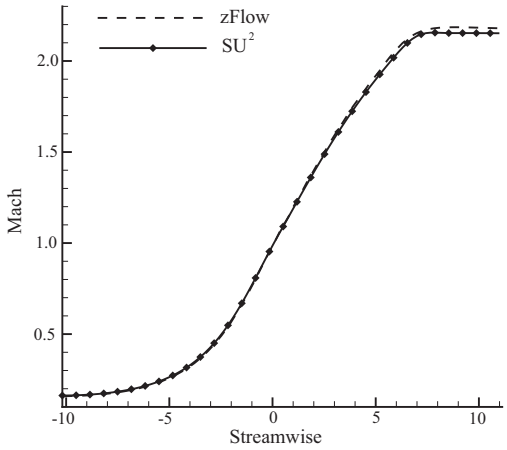

Figure 3. Sampling of the Mach value along the symmetry plane.

Fluid	MDM
Thermodynamic model	Span-Wagner
Total inlet temperature	592.1 K
Total inlet pressure	13.87 bar
Static outlet pressure	11.00 bar
Molecular viscosity	1.3764E-5 Pa × s
Thermal conductivity	0.047280 W/m/K
Spatial scheme	Upwind generalized Roe 2nd order
Turbulence Model	SA
Inlet turbulence intensity	0.05

Table 2. Input data for the LS89 turbine cascade simulation.

The working fluid is perfluorocarbon PP90, modeled with the polytropic Peng-Robinson equation of state and constant transport properties. Table 3 summarizes the parameters of the simulation. A commercial software[35] (CS) is here used as benchmark by coherently specifying the same thermo-physical models.
Figures 10 and 11 visualize the Mach flow fields evolution at center meridional and bottom surface, respectively. The abrupt termination of the wedge causes a sudden flow detachment and a clearly visible zone of recirculation. Seemingly, the two codes predict a rather different wake arrangement downstream of the wedge, though the same turbulence model is adopted. A solid motivation of this fact would entail a full understanding of the characteristics of CS, which is normally hard to acquire for black-box commercial package. Qualitatively, SU2 is less diffusive than CS, i.e. shock discontinuities are captured with greater intensity as shown in Fig. 10. To quantitatively assess the deviation of the two solutions, streamwise evolution of density, pressure, and Mach number is reported in Fig. 12, 13, and 14. The quantities are sampled following a line intersecting the oblique shock and the expansion fan at wedge tip, such that the most critical flow features are simultaneously taken into account. Marginal deviations are found for pressure and density, whereas the Mach number significantly differs downstream of the oblique shock. This remarkable discrepancy may be consequence of the higher diffusivity of the CS solver that induces a weaker shock wave at wedge leading-

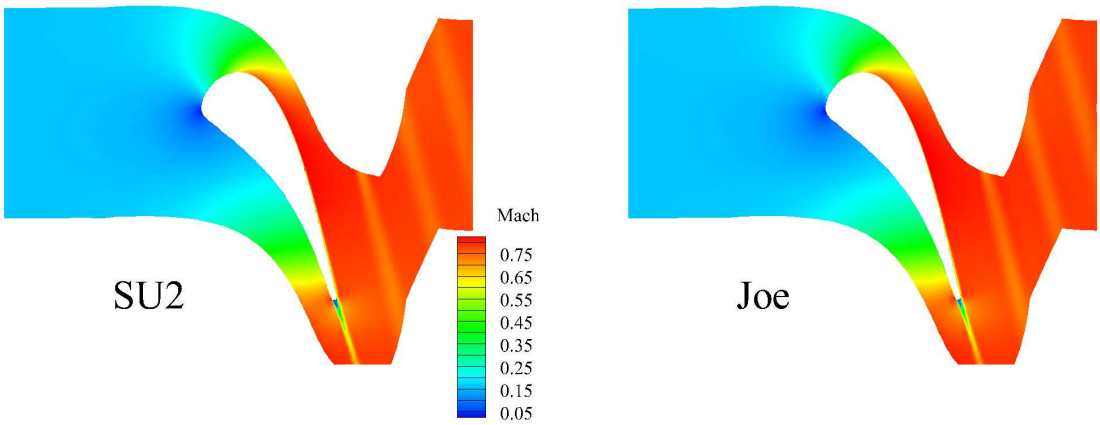

Figure 4. SU2 and Joe Mach number contours of the LS89.

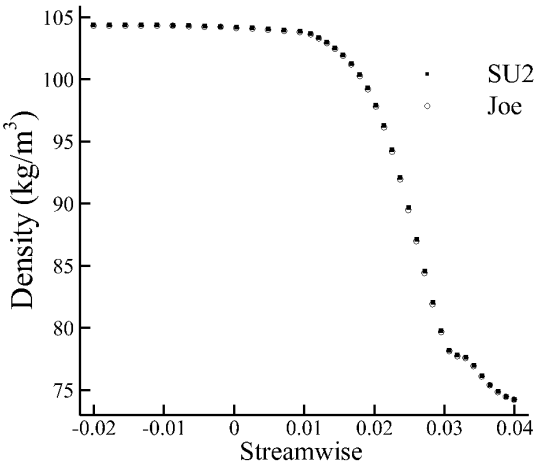

Figure 5. Density evolution in the turbine channel.

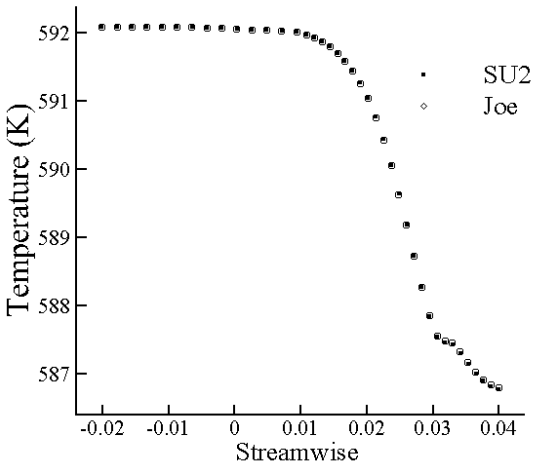

Figure 6. Temperature evolution in the turbine channel.

edge and a less pronounced flow velocity peak when crossing the expansion fan. However, the results of the comparison attest that SU2 can now effectively simulate fully 3D turbulent flow of dense vapors.

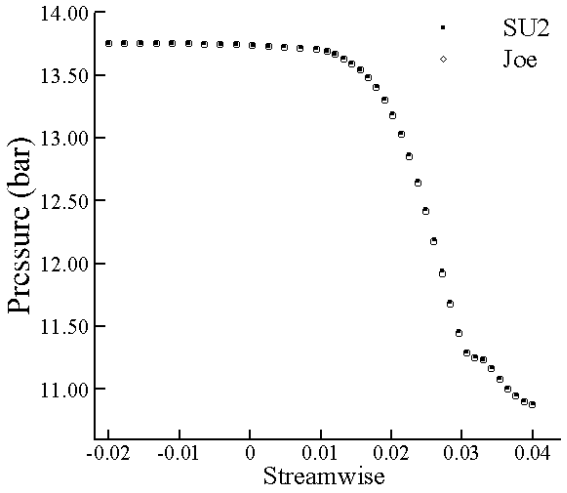

Figure 7. Pressure evolution in the turbine channel.

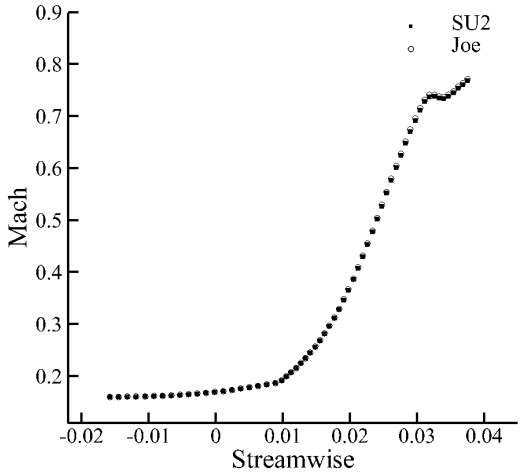

Figure 8. Mach number evolution in the turbine channel.

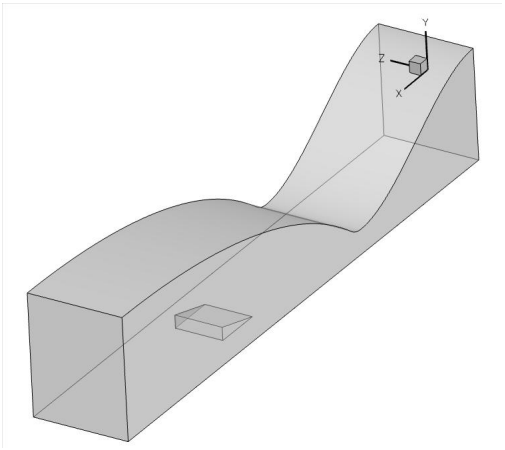

Figure 9. Computational domain of the 3D supersonic nozzle with a wedge in the supersonic region.

Fluid	PP90
Thermodynamic model	PPR
Gas Constant	17.03 J/K/kg
Specific heat ratio	1.0186
Critical temperature	530.00 K
Critical pressure	16.00 bar
Acentric Factor	0.5621
Total inlet temperature	538.15 K
Total inlet pressure	17.512 bar
Molecular viscosity	2.4087E-5 Pa $\times$ s
Thermal conductivity	0.0260 W/m/K
Turbulence model	SST-kω
Inlet turbulence intensity	0.05
Spatial scheme	Upwind generalized Roe 2nd order

Table 3. Main parameters of the 3D supersonic nozzle simulation.

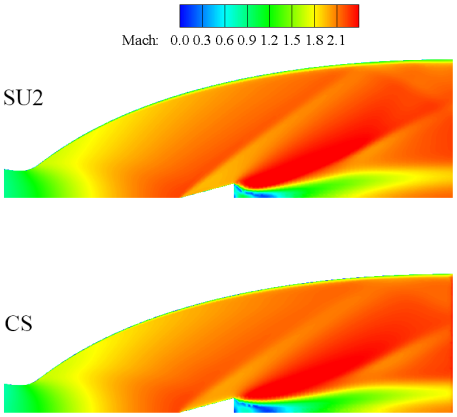

Figure 10. Mach contours of a central section of the nozzle in the supersonic flow region.

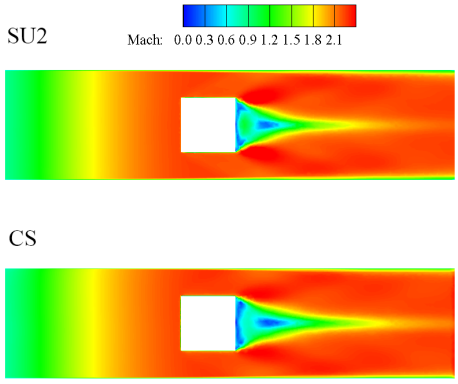

Figure 11. Mach contours of a bottom section of the nozzle in the supersonic flow region.

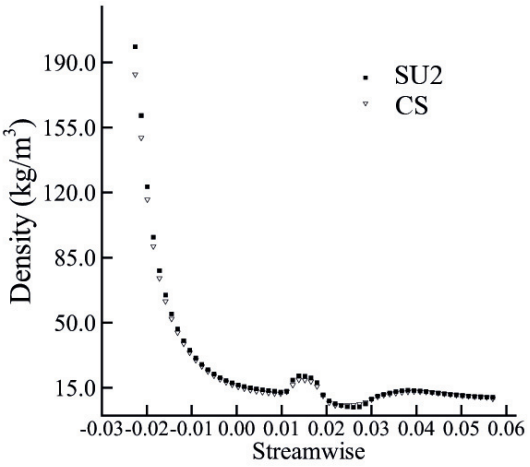

Figure 12. Density distribution through the shock waves and the wake in the supersonic flow region.

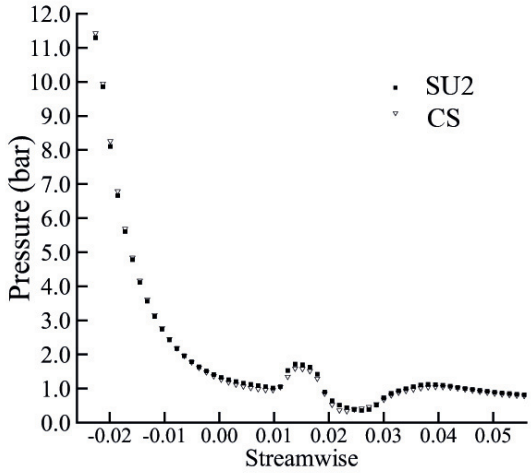

Figure 13. Pressure distribution through the shock waves and the wake in the supersonic flow region.

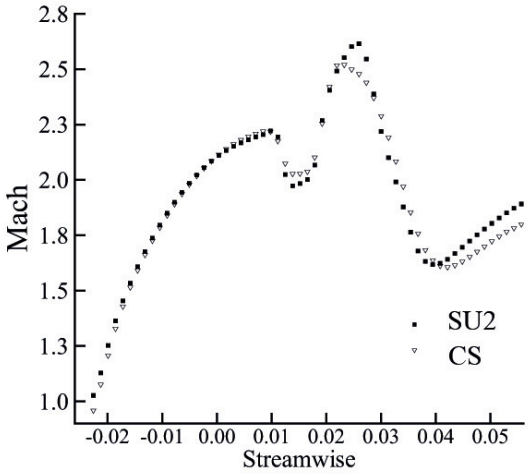

Figure 14. Mach distribution through the shock waves and the wake in the supersonic flow region.

D. Rarefaction shock-wave

In thermodynamic conditions close to the critical point some particular fluids show a non-classical behavior. For example fluids belonging to MD_nM class are supposed, by theory, to produce non-classical gas dynamic phenomena such as rarefaction shock waves or compression fans. In particular, for these specific fluid, the Van der Waals equation of state allows the mentioned phenomena to be predicted. The fluid considered in this section is a MDM siloxane and its properties are enlisted in Table 4.

Critical pressure	14.152 bar
Critical temperature	564.1 K
Critical density	256.82 kg/m^3
γ	1.0125
Gas constant	35.152 J/kg/K
Acentric factor	0.529

Table 4. MDM thermodynamic properties.

Results here presented were obtained assuming fluid conditions to be close to critical point, in order to show and highlight non-classical phenomena.
Table 5 resumes the imposed fluid conditions at the inlet.

Pressure	15.001 bar
Density	202.89 kg/m^3
Mach	1.7

Table 5. Fluid conditions at the inlet.

The geometry consist of a simple square domain containing an edge with a defined slope $\theta = 15.945°$, and the fluid flows through the domain from the left to the right boundary. A symmetry condition is applied at the upper border, while at the bottom surface holds an inviscid wall boundary condition.

1. Polytropic Ideal gas

In case that the PIG is used to model the fluid, this particular problem can be solved analytically through the well-known Prandtl-Meyer expansion function.
By means of the Prandtl-Meyer relation is possible to compute an analytical mach value $M_2 = 2.037298$. Simulation using SU2 with a PIG fluid model predicts an after-expansion Mach number of 2.03728, which is respectful of the theoretical value up to the 4th decimal. The first characteristic wave has a theoretical inclination, with respect to the horizontal surface, of 36.031° instead of the 34.871° computed using SU2. The theoretical value for the Mach angle between the surface of the ramp and the last expansion wave is 29.396° while the computed angle is 30.0274°. Predicted expansion compare fairly well with theoretical solution, small errors are possibly related to numerical approximation bounded to the partition of the computational domain.

2. Polytropic Van der Waals

The Wan der Waals EoS (Equation of State) is now used instead of the perfect gas law. Condition are the same as those listed in Table 5 and were chosen properly to enter the thermodynamic region where non-classical gas-dynamic phenomena occur. Results clearly show the existence of a non-classical rarefaction shock wave. Dimensionless variables with respect to the critical values of the fluid, before and after the rarefaction shock-wave, are reported in Table 6. From now on, we identify the fluid state before the shock with the subscript 1 and the state after the shock with the subscript 2. The angle β is now defined as the angle between the shock-wave and the direction of the x-axis.
Rankine-Hugoniot condition across the shock for Van der Waals EoS states that:

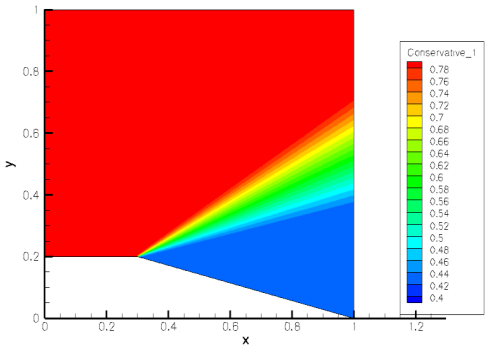

Figure 15. Ideal gas: density

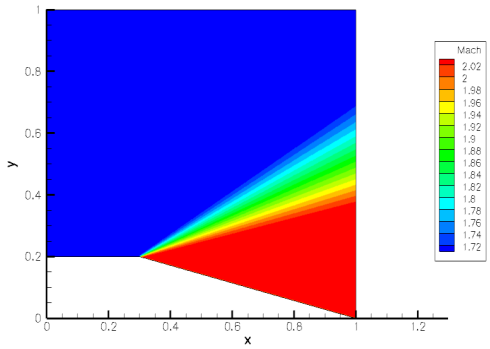

Figure 16. Ideal gas: Mach number

	Before	After
Density	0.79	0.446473
Pressure	1.06	0.9287
Mach	1.7	1.188
Temperature	1.0135	1.00362
Total energy	287.8165	287.04087
Sound speed	0.504	0.0433

Table 6. Fluid state before and after the rarefaction shock-wave.

$$h_2 - h_1 = (e_2 + p_2 v_2) - (e_1 + p_1 v_1) = \frac{1}{2}(p_2 - p_1)(v_2 - v_1). \tag{22}$$

By substituting the expression of internal energy for a Van der Waals gas and rearranging, Rankine-Hugoniot condition become:

$$p_2 = \frac{\dfrac{v_1 - b}{\gamma - 1}\left(p_1 + \dfrac{a}{v_1^2}\right) - \dfrac{a}{v_1} - \dfrac{p_1}{2}(v_2 - v_1) + a\left(1 - \dfrac{1}{\gamma - 1}\right)\dfrac{1}{v_2} + \dfrac{ab}{(\gamma - 1)\, v_2^2}}{\left(\dfrac{1}{2} + \dfrac{1}{\gamma - 1}\right) v_2 - \left(\dfrac{v_1}{2} + \dfrac{b}{\gamma - 1}\right)}. \tag{23}$$

From value listed in Table 6 it follows that the percentage error between the computed and the theoretical value for p_2 is $5.3163 \cdot 10^{-5}$

From theory is possible to compute the analytical value of the angle β which depends only on the thermodynamic state of the fluid before and after the shock, this relation reads:

$$\beta = \arcsin\sqrt{\frac{p_2 - p_1}{\rho_2 - \rho_1}\frac{\rho_2}{\rho_1}\frac{1}{c_1^2 M_1^2}}. \tag{24}$$

Which in the discussed case returns a value of $\beta = 32.8602°$. The computed shock angle is instead $\beta = 32.735°$ which is fairly close to the theoretical value.

Figures from 19 to 26 show density and Mach number distribution for meshes composed by an increasing number of element (see Table 7).

mesh	A	B	C	D	E	F
N elements	2301	5251	14751	49551	104351	179151

Table 7. Number of elements composing each mesh.

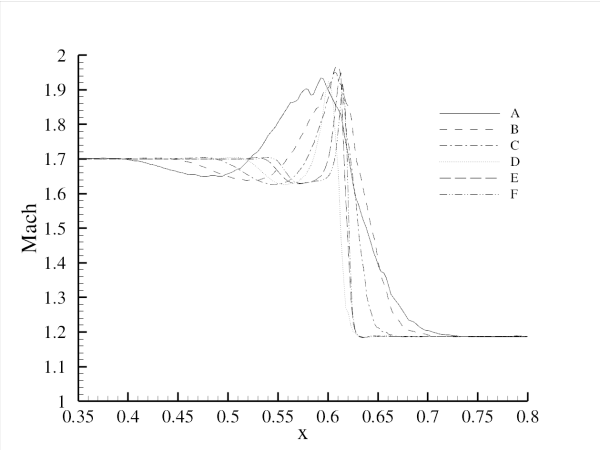

Figure 17. Mach profile along $y = 0.4$ for all domains tested.

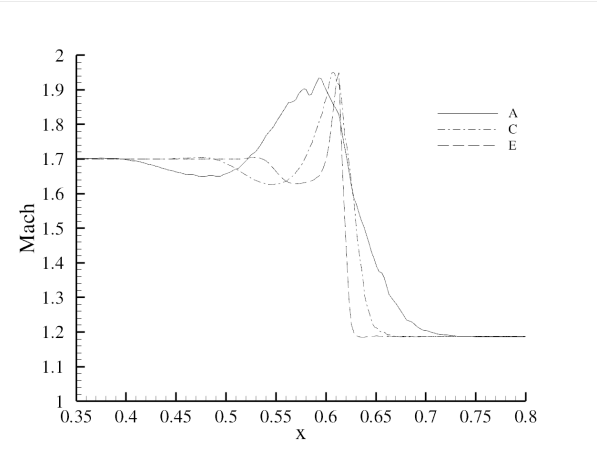

Figure 18. Mach profile along $y = 0.4$ only for the domains A,C and E.

In Fig. 17 Mach profile along $y = 0.4$ ordinate are plotted for all meshes. It is possible to note how the shock is better captured when the mesh is refined. In Fig. 18 Mach profiles are plotted for mesh A, C and E: the discontinuity appears to be smeared on a wider region in the case of A with respect to E. As expected with a higher space resolution the shock is better represented. Because of gas non-ideality, this transition occurs via a non-monotone variation of the Mach number across the shock.

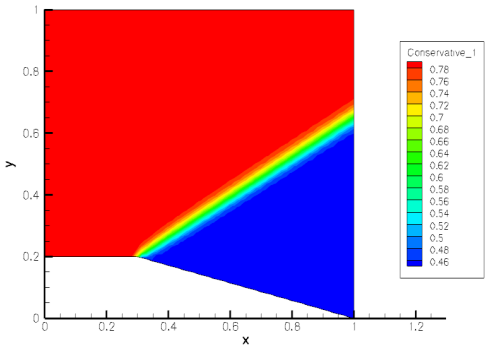

Figure 19. Van der Waals, case A: density

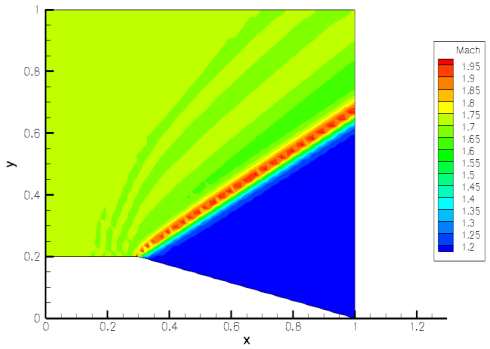

Figure 20. Van der Waals, case A: Mach

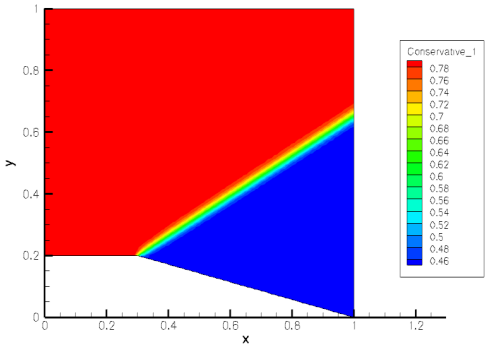

Figure 21. Van der Waals, case B: density

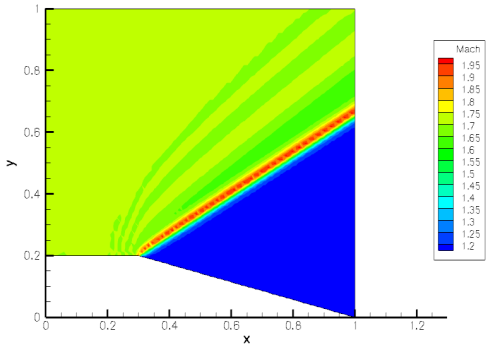

Figure 22. Van der Waals, case B: Mach

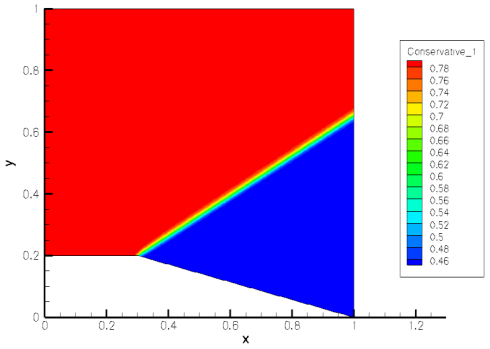

Figure 23. Van der Waals, case C: density

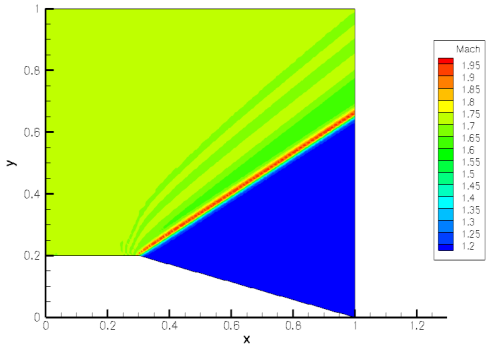

Figure 24. Van der Waals, case C: Mach

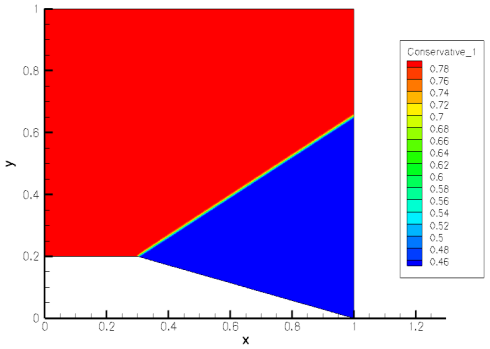

Figure 25. Van der Waals, case E: density

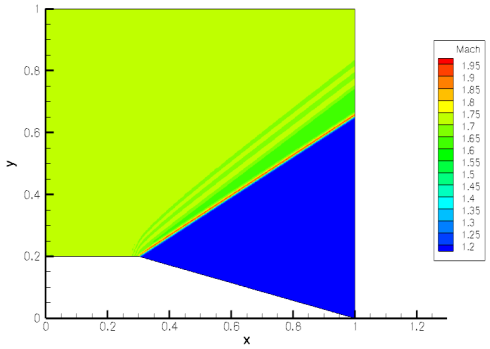

Figure 26. Van der Waals, case E: Mach

V. Conclusions

In this work, we have prepared SU2 for simulating non-ideal compressible fluid flows with arbitrary thermophysical models, and we have verified the capability of the new software suite against other well-established NICFD codes, and known analytical solutions based on the theory of non-classical gas-dynamics. The results achieved have shown that SU2 is now ready to be used for high fidelity turbulent flow analysis for supercritical fluid and dense vapor conditions. The new features have been integrated in the previous SU2 release according to its programming paradigm, and represent an additional brick towards an open-source reliable simulation environment for multi-physics problems. In order to cope with highly complex equations of state, the infrastructure is now interfaced with external library, which will allow also the modeling of equilibrium two-phase flow.
As future step, the worthwhile collaboration of the three research groups will lead to progressively enrich the capability of the suite. End-to-end turbomachinery simulations close to the critical point, non-equilibrium two-phase flow prediction, and adjoint-based design methodologies with complex thermophysical models are planned and expected in the upcoming years.

VI. Acknowledgements

Salvatore Vitale would like to acknowledge his colleague A.J. Head and the support of the STW and Dana Spicer on the CC-Powertrain project. Alberto Guardone and Giulio Gori would like to acknowledge the European Research Council (ERC) of the European Research Council Executive Agency.

Appendix A: Generalized spatial schemes

The jacobian A_c of the physical convective flux derived respect the conservative variables:

$$A_\mathrm{c} = \begin{bmatrix} 0 & n_1 & n_2 & n_3 & 0 \\ -v_1 q_n + \zeta n_1 & q_n + v_1 n_1 - \kappa n_1 v_1 & v_1 n_2 - \kappa n_1 v_2 & v_1 n_3 - \kappa n_1 v_3 & \kappa n_1 \\ -v_2 q_n + \zeta n_2 & v_2 n_1 - \kappa n_2 v_1 & q_n + v_2 n_2 - \kappa n_2 v_2 & v_2 n_3 - \kappa n_2 v_3 & \kappa n_2 \\ -v_3 q_n + \zeta n_3 & v_3 n_1 - \kappa n_3 v_1 & v_3 n_2 - \kappa n_3 v_2 & q_n + v_3 n_3 - \kappa n_3 v_3 & \kappa n_3 \\ (\zeta - H) q_n & H n_1 - \kappa v_1 q_n & H n_2 - \kappa v_2 q_n & H n_3 - \kappa v_3 q_n & (1+\kappa) q_n \end{bmatrix} \tag{25}$$

where

$$\zeta = \left(\chi + \frac{1}{2} \kappa \left| v \right|^2 \right) \tag{26}$$

$$q_n = v_1 n_1 + v_2 n_2 + v_3 n_3 \tag{27}$$

P and P^{-1} are respectively the right and the left eigenvectors of the Jacobian.

$$P = \begin{bmatrix} n_1 & n_2 & n_3 & \frac{1}{2}\frac{\rho}{c} & \frac{1}{2}\frac{\rho}{c} \\ v_1 n_1 & v_1 n_2 - \rho n_3 & v_1 n_3 + \rho n_2 & \sigma_1^+ & \sigma_1^- \\ v_2 n_1 + \rho n_3 & v_2 n_2 & v_2 n_3 - \rho n_1 & \sigma_2^+ & \sigma_2^- \\ v_3 n_1 - \rho n_2 & v_3 n_2 + \rho n_1 & v_3 n_3 & \sigma_3^+ & \sigma_3^- \\ \psi_1 + \rho(v_2 n_3 - v_3 n_2) & \psi_2 + \rho(v_3 n_1 - v_1 n_3) & \psi_3 + \rho(v_1 n_2 - v_2 n_1) & \varphi^+ & \varphi^- \end{bmatrix} \tag{28}$$

$$\psi_\mathrm{i} = \left(\left| v \right|^2 - \frac{\zeta}{\kappa} \right) n_\mathrm{i} \tag{29}$$

$$\sigma_\mathrm{i}^\pm = \frac{1}{2} \left(\frac{\rho}{c} v_\mathrm{i} \pm \rho n_\mathrm{i} \right) \tag{30}$$

$$\varphi^\pm = \frac{1}{2} \left(\frac{\rho}{c} H \pm \rho q_n \right) \tag{31}$$

$$P^{-1} = \begin{bmatrix} \left(1-\frac{\zeta}{c^2}\right)n_1 - \frac{v_2}{\rho}n_3 + \frac{v_3}{\rho}n_2 & \frac{v_1\kappa}{c^2}n_1 & \frac{v_2\kappa}{c^2}n_1 + \frac{1}{\rho}n_3 & \frac{v_3\kappa}{c^2}n_1 - \frac{1}{\rho}n_2 & -\frac{\kappa}{c^2}n_1 \\ \left(1-\frac{\zeta}{c^2}\right)n_2 - \frac{v_3}{\rho}n_1 + \frac{v_1}{\rho}n_3 & \frac{v_1\kappa}{c^2}n_2 - \frac{1}{\rho}n_3 & \frac{v_2\kappa}{c^2}n_2 & \frac{v_3\kappa}{c^2}n_2 + \frac{1}{\rho}n_1 & -\frac{\kappa}{c^2}n_2 \\ \left(1-\frac{\zeta}{c^2}\right)n_3 - \frac{v_1}{\rho}n_2 + \frac{v_2}{\rho}n_1 & \frac{v_1\kappa}{c^2}n_3 + \frac{1}{\rho}n_2 & \frac{v_2\kappa}{c^2}n_3 - \frac{1}{\rho}n_1 & \frac{v_3\kappa}{c^2}n_3 & -\frac{\kappa}{c^2}n_3 \\ \frac{\zeta}{\rho c} - \frac{q_n}{\rho} & -\frac{v_1\kappa}{\rho c} + \frac{1}{\rho}n_1 & -\frac{v_2\kappa}{\rho c} + \frac{1}{\rho}n_2 & -\frac{v_3\kappa}{\rho c} + \frac{1}{\rho}n_3 & \frac{\kappa}{\rho c} \\ \frac{\zeta}{\rho c} + \frac{q_n}{\rho} & -\frac{v_1\kappa}{\rho c} - \frac{1}{\rho}n_1 & -\frac{v_2\kappa}{\rho c} - \frac{1}{\rho}n_2 & -\frac{v_3\kappa}{\rho c} - \frac{1}{\rho}n_3 & \frac{\kappa}{\rho c} \end{bmatrix} \tag{32}$$

δw are the characteristic variables and Λ is the eigenvalues matrix

$$\delta v = P^{-1}\delta U \begin{pmatrix} \delta\rho - \frac{\delta P}{c^2} \\ n_1 v_3 - n_3 v_0 \\ n_2 v_1 - n_1 v_2 \\ \frac{\delta P}{c\rho} + q_n \\ \frac{\delta P}{c\rho} - q_n \end{pmatrix} \tag{33}$$

$$\Lambda = \begin{bmatrix} q_n & 0 & 0 & 0 & 0 \\ 0 & q_n & 0 & 0 & 0 \\ 0 & 0 & q_n & 0 & 0 \\ 0 & 0 & 0 & q_n + c & 0 \\ 0 & 0 & 0 & 0 & q_n - c \end{bmatrix}. \tag{34}$$

Appendix B: thermodynamic models

A. Perfect gas

The set of equations, describing the volumetric and caloric behavior of a polytropic ideal gas (PIG), can be written as

$$\begin{cases} p\left(T,v\right) = \dfrac{RT}{v} \\ e\left(T,v\right) = e\left(T\right) = e_{\text{ref}} + c_v\left(T - T_{\text{ref}}\right) \\ s\left(T,v\right) = s_{\text{ref}} + c_v \ln\frac{T}{T_{\text{ref}}} + R\ln\frac{v}{v_{\text{ref}}} \\ c_v = \frac{1}{\gamma-1}R \end{cases} \tag{35}$$

Where $\gamma = \frac{C_p}{C_v}$ is the specific heat ratio. Reference values for energy and entropy are defined as:

$$\begin{cases} e_{\text{ref}} = c_v T_{\text{ref}} \\ s_{\text{ref}} = -c_v \ln T_{\text{ref}} + R\ln v_{\text{ref}} \end{cases} \tag{36}$$

T_{ref} and v_{ref} together with p_{ref} are defined by the user to non-dimensionalize the problem. This approach simplifies the implementation of the equations of entropy and energy:

$$\begin{cases} e\left(T,v\right) = c_v T \\ s\left(T,v\right) = c_v \ln T + R\ln v \end{cases} \tag{37}$$

Thermodynamic Derivatives

Four secondary properties are needed for computing the numerical schemes. For a PIG gas they can be written as

$$\left(\frac{\partial p}{\partial e}\right)_{\rho} = (\gamma - 1)\cdot\rho \tag{38}$$

$$\left(\frac{\partial p}{\partial \rho}\right)_e = (\gamma - 1) \cdot e \tag{39}$$

$$\left(\frac{\partial T}{\partial e}\right)_\rho = \frac{(\gamma - 1)}{R} \tag{40}$$

$$\left(\frac{\partial T}{\partial \rho}\right)_e = 0. \tag{41}$$

and speed of sound can be more generally recovered as a combination of the first two properties as:

$$c^2 = \left(\frac{\partial p}{\partial \rho}\right)_e + \frac{p}{\rho^2}\left(\frac{\partial p}{\partial e}\right)_\rho \tag{42}$$

B. Van der Waals

The equations of a polytropic Van der Waals gas (PVdW) model are:

$$\begin{cases} p\left(T, v\right) = \dfrac{RT}{v - b} - \dfrac{a}{v^2} \\ e\left(T, v\right) = c_v T - \dfrac{a}{v} \\ s\left(T, v\right) = c_v \ln T + R \ln\left(v - b\right) \end{cases} \tag{43}$$

where a represent a measure of the intensity of the inter-molecular attractive force while b is the covolume. Both these two values are supposed to be constant and depend from the chemical composition of the gas:

$$\begin{cases} a = \frac{27}{64}\frac{R^2 T_{\text{cr}}^2}{P_{\text{cr}}} \\ b = \frac{1}{8}\frac{RT_{\text{cr}}}{P_{\text{cr}}} \end{cases} \tag{44}$$

T_{cr} and P_{cr} are the critical temperature and pressure respectively. Notice that for consistency the equations of the energy and entropy use the same e_{ref} and s_{ref}, defined in Eq. 36.

Thermodynamic Derivatives

For a Van der Waals gas the secondary properties are given by:

$$\left(\frac{\partial p}{\partial e}\right)_\rho = \frac{\rho\left(\gamma - 1\right)}{1 - \rho b} \tag{45}$$

$$\left(\frac{\partial p}{\partial \rho}\right)_e = \frac{\left(e + 2\rho a - \rho^2 a b\right)}{\rho\left(1 - \rho b\right)}\left(\frac{\partial p}{\partial e}\right)_\rho - 2\rho a \tag{46}$$

$$\left(\frac{\partial T}{\partial e}\right)_\rho = \frac{(\gamma - 1)}{R} \tag{47}$$

$$\left(\frac{\partial T}{\partial \rho}\right)_e = \frac{1}{a}\left(\frac{\partial T}{\partial e}\right)_\rho \tag{48}$$

Finally the speed of sound is computing using Eq. 42.

C. Peng-Robinson

Peng-Robinson proposed their non-ideal gas model in 1976. Basically, the model modifies the SRK ($Soave-Redlich-Kwong$) equation of state to improve the prediction of liquid density values, vapor pressures, and equilibrium ratios. The polytropic Peng Robinson model can be conveniently written as

$$\begin{cases} p\left(T,v\right)=\dfrac{RT}{v-b}-\dfrac{a\alpha^{2}\left(T\right)}{v^{2}+2bv-b^{2}} \\ e\left(T,v\right)=c_{v}T-\frac{a\alpha(T)(k+1)}{b\sqrt{2}}\tanh^{-1}\dfrac{b\sqrt{2}}{v+b} \\ s\left(T,v\right)=c_{v}lnT+R\ln\left(v-b\right)-\dfrac{a\alpha\left(T\right)k}{b\sqrt{2TT_{\mathrm{cr}}}}\tanh^{-1}\dfrac{b\sqrt{2}}{v+b}, \end{cases} \tag{49}$$

whereby $\alpha\left(T\right)$ represents the inter-molecular attraction force, which depends on the temperature T, while a and b are usually treated as temperature independent. Their values are calculated as follows:

$$\begin{cases} a=0.45724\frac{\left(RT_{\mathrm{cr}}\right)^{2}}{P_{\mathrm{cr}}} \\ b=0.0778\frac{RT_{\mathrm{cr}}}{P_{\mathrm{cr}}} \\ \alpha\left(T,\omega\right)=\left[1+k\left(1-\sqrt{\dfrac{T}{T_{\mathrm{cr}}}}\right)\right] \\ k=\begin{cases} 0.37464+1.54226\omega-0.26992\omega^{2} & \omega\leq0.49 \\ 0.379642+1.48503\omega-0.164423\omega^{2}+0.016666\omega^{3} & \omega>0.49 \end{cases} \end{cases} \tag{50}$$

Again for matters of consistency the energy and the entropy equations use the same e_{ref} and s_{ref}, defined in Eq. 36.

Thermodynamic Derivatives

For a Peng-Robinson gas the secondary properties are given by:

$$\left(\frac{\partial p}{\partial e}\right)_{\rho}=\frac{\left(\dfrac{\partial p}{\partial T}\right)_{\rho}}{\left(\dfrac{\partial e}{\partial T}\right)_{\rho}} \tag{51}$$

$$\left(\frac{\partial p}{\partial\rho}\right)_{e}=\left(\frac{\partial p}{\partial\rho}\right)_{T}-\left(\frac{\partial p}{\partial e}\right)_{\rho}\left(\frac{\partial e}{\partial\rho}\right)_{T} \tag{52}$$

$$\left(\frac{\partial T}{\partial e}\right)_{\rho}=\frac{1}{\left(\dfrac{\partial e}{\partial T}\right)_{\rho}} \tag{53}$$

$$\left(\frac{\partial T}{\partial\rho}\right)_{e}=\left(\frac{\partial T}{\partial\rho}\right)_{p}-\left(\frac{\partial T}{\partial p}\right)_{\rho}\frac{\left(\frac{\partial e}{\partial T}\right)_{p}}{\left(\frac{\partial\rho}{\partial T}\right)_{p}} \tag{54}$$

where

$$\left(\frac{\partial p}{\partial T}\right)_{\rho}=\frac{R}{\left(v-b\right)}-\frac{2a\alpha\alpha'}{\left[v\left(v+b\right)+b\left(v-b\right)\right]},\qquad\alpha'=\frac{d\alpha}{dT} \tag{55}$$

$$\left(\frac{\partial e}{\partial T}\right)_{\rho}=\frac{R}{\gamma-1}-\frac{a}{b\sqrt{2}}\left[2\alpha\alpha'+k\alpha'\sqrt{\frac{T}{T_{c}}}+\frac{1}{2}k\alpha\left(TT_{C}\right)^{-\frac{1}{2}}\right]f\left(v\right) \tag{56}$$

$$\left(\frac{\partial p}{\partial\rho}\right)_{T}=-\frac{1}{\rho^{2}}\left(\frac{\partial p}{\partial v}\right)_{T}=-\left(-\frac{RT}{\left(v-b\right)^{2}}+\frac{2a\alpha^{2}\left(v+b\right)}{\left[v\left(v+b\right)+b\left(v-b\right)\right]^{2}}\right)v^{2} \tag{57}$$

$$\left(\frac{\partial e}{\partial \rho}\right)_T = \frac{\partial}{\partial \rho}\left(-\frac{a\alpha\left(T\right)}{b\sqrt{2}}\left[\alpha\left(T\right)+k\sqrt{\frac{T}{T_c}}\right]\tanh^{-1}\frac{b\sqrt{2}}{v+b}\right) = -\frac{a\alpha\left(T\right)}{b\sqrt{2}}\left[\alpha\left(T\right)+k\sqrt{\frac{T}{T_c}}\right]\frac{b\sqrt{2}}{1+2\rho b-\rho^2 b^2} \tag{58}$$

$$\left(\frac{\partial \rho}{\partial T}\right)_p = -\rho^2\left(\frac{\partial v}{\partial T}\right)_p \tag{59}$$

$$\left(\frac{\partial T}{\partial \rho}\right)_p = \frac{1}{\left(\frac{\partial \rho}{\partial T}\right)_p} \tag{60}$$

$$\left(\frac{\partial v}{\partial T}\right)_p = -\left[\left(\frac{\partial p}{\partial v}\right)_T\left(\frac{\partial T}{\partial p}\right)_v\right]^{-1} = -\left(\frac{\partial p}{\partial v}\right)_T^{-1}\left(\frac{\partial p}{\partial T}\right)_v \tag{61}$$

$$\left(\frac{\partial e}{\partial T}\right)_p = \left(\frac{\partial h}{\partial T}\right)_p - p\left(\frac{\partial v}{\partial T}\right)_p \tag{62}$$

$$\left(\frac{\partial h}{\partial T}\right)_p = \left(\frac{\partial e}{\partial T}\right)_v + T\left(\frac{\partial p}{\partial T}\right)_v\left(\frac{\partial v}{\partial T}\right)_p \tag{63}$$

Finally the speed of sound is computing using the general expression in Eq. 42.

References

[1]F. Palacios, M. R. Colonno, A. C. Aranake, A. Campos, S. R. Copeland, T. D. Economon, A. K. Lonkar, T. W. Lukaczyk, T. W. R. Taylor, and J. J. Alonso. Stanford University Unstructured (SU^2): An open-source integrated computational environment for multi-physics simulation and design. *AIAA Paper 2013-0287*, 51st AIAA Aerospace Sciences Meeting and Exhibit, January 2013.

[2]P. Colonna and A. Guardone. Molecular interpretation of nonclassical gas dynamics of dense vapors under the van der Waals model. *Physics of Fluids*, 18:056101–14, 2006.

[3]P. Colonna, A. Guardone, and N. R. Nannan. Siloxanes: a new class of candidate Bethe-Zeldovich-Thompson fluids. *Physics of Fluids*, 19, 2007.

[4]N.R. Nannan, A. Guardone, and P. Colonna. Critical point anomalies include expansion shock waves. *Physics of Fluids*, 26:021701–7, 2014.

[5]U. Drescher and D. Bruggeman. Fluid selection for the Organic Rankine Cycle (ORC) in biomass power and heat plants. *Applied Thermal Engineering*, 27(1):223–228, 2007.

[6]W. Lang, R. Almbauer, and P. Colonna. Assessment of Waste Heat Recovery for A Heavy-duty Truck Engine Using An ORC Turbogenerator. *Journal of Engineering for Gas Turbines and Power-Transactions of the ASME*, 135(4):042313–1–10, 2013.

[7]Sylvain Quoilin, Martijn Van Den Broek, Sébastien Declaye, Pierre Dewallef, and Vincent Lemort. Techno-economic survey of Organic Rankine Cycle (ORC) systems. *Renewable and Sustainable Energy Reviews*, 22(0):168–186, 2013.

[8]E. Casati, S. Vitale, M. Pini, G. Persico, and P. Colonna. Centrifugal Turbines for Mini-Organic Rankine Cycle Power Systems. *Journal of Engineering for Gas Turbines and Power*, 136:122607–1–11, 2014.

[9]C. Lettieri, N. Baltadjiev, M Casey, and Z. Spakovszky. Low-Flow-Coefficient Centrifugal Compressor Design for Supercritical CO_2. *Journal of Turbomachinery*, 136:081008–1–9, 2014.

[10]C. Lettieri, D. Yang, and Z. Spakovszky. An Investigation of Condensation Effects in Supercritical Carbon Dioxide Compressors. In *The 4th International Symposium - Supercritical CO_2 Power Cycles*, September 2014.

[11]V. Dostal, P. Hejzlar, and M.J. Driscoll. The supercritical carbon dioxide power cycle: comparison to other advanced power cycles. *Nuclear technology*, 154(3), 283-301.

[12]B. Subramaniam, R.A. Rajewski, and K. Snavely. Pharmaceutical processing with supercritical carbon dioxide. *Journal of Pharmaceutical Sciences*, 86(8), August 1997.

[13]W. Bober and W.L. Chow. Nonideal Isentropic Gas Flow Through Converging-Diverging Nozzles. *Journal of Fluids Engineering*, 112(4):455–460, 1990.

[14]A. Guardone, A. Spinelli, and V. Dossena. Influence of Molecular Complexity on Nozzle Design for an Organic Vapor Wind Tunnel. *ASME Journal of Engineering for Gas Turbines and Power*, 135, 2013.

[15]P. Colonna and S. Rebay. Numerical simulation of dense gas flows on unstructured grids with an implicit high resolution upwind Euler solver. *International Journal for Numerical Methods in Fluids*, 46:735–765, 2004.

[16]P. Colonna, J. Harinck, S. Rebay, and A. Guardone. Real-gas effects in Organic Rankine Cycle turbine nozzles. *Journal of Propulsion and Power*, 24, issue 2:282–294, 2008.

[17]E. Rinaldi, R. Pecnik, and P. Colonna. Exact Jacobians for implicit Navier-Stokes simulations of equlibrium real gas flows. *Journal of Computational Physics*, 270:459–477, 2014.

[18]J. Harinck, T. Turunen-Saaresti, P. Colonna, S. Rebay, and J.P. Van Buijtenen. Computational study of a high-expansion ratio radial ORC turbine stator. *Journal of Engineering for Gas Turbines and Power*, 132, 2010.

[19]J. Harinck, P. Colonna, A. Guardone, and S. Rebay. Influence of thermodynamic models in 2D flow simulations of turboexpanders. *Journal of Turbomachinery*, 132, 2010.

[20]P. Colonna and T.P. van der Stelt. FluidProp: A program for the estimation of thermo-physical properties of fluids. Technical report, 2005.

[21]J.L. Montagne, H.C. Yee, and M. Vinokur. Comparative Study of High-Resolution Shock-CapturingSchemes for a Real Gas. *AIAA Journal*, 27(10):1332–1346, 1989.

[22]J.L. Montagne and M. Vinokur. Generalized flux-vector splitting and Roe average for an equilibrium real gas. *Journal of Computational Physics*, 89(2):276–300, 1990.

[23]L.D. Landau and E.M. Lifshitz. *Fluid Mechanics (2nd Edition)*. Pergamon Press, 1993.

[24]D.C. Wilcox. *Turbulence Modeling for CFD*. 2nd Ed., DCW Industries, Inc., 1998.

[25]A. Guardone and L. Vigevano. Roe Linearization for the van der Waals Gas. *Journal of Computational Physics*, 175(10):50–78, 2002.

[26]P. Cinnella. Roe-type schemes for dense gas flow computations. *Computers & Fluids*, 35(10):1264–1281, 2006.

[27]P. Glaister. An approximate linearised riemann solver for the Euler equations for real gases. *Journal of Computational Physics*, 74(2):382–408, 1988.

[28]B. van Leer. Towards the ultimate conservative difference scheme V. a second-order sequel to Godunov's method. *Journal of Computational Physics*, 32(1):101–136, July 1979.

[29]T.H. Pulliam and J.L. Steger. Recent improvements in efficiency, accuracy, and convergence for implicit approximate factorization algorithms. In *AIAA 3rd Aerospace Sciences Meeting*, volume AIAA-85-0360, 1985.

[30]J. Blazek. *Computational Fluid Dynamics: Principles and Applications*. Elsevier, Oxford, 2005.

[31]A. Guardone, D. Isola, and G. Quaranta. Arbitrary Lagrangian Eulerian formulation for two-dimensional flows using dynamic meshes with edge swapping. *Journal of Computational Physics*, 230(20):7706–7722, 2011.

[32]M. Pini, A. Spinelli, G. Persico, and S. Rebay. Consistent Look-up Table Interpolation Method for Real-Gas Flow Simulations. *submitted to Computers & Fluids*, 2014.

[33]R. Span and W. Wagner. Equations of State for Technical Applications. I. Simultaneously Optimized Functional Forms for Nonpolar and Polar Fluids. *International Journal of Thermophysics*, 24(1):1–39, January 2003.

[34]R. Pecnik, V. E. Terrapon, F. Ham, G. Iaccarino, and H. Pitsch. Reynolds-Averaged Navier-Stokes Simulations of the HyShot II Scramjet. *AIAA Journal*, 50(8):1717–1732, 2012.

[35]Release 14.0 ANSYS Inc. Academic Research. *CFX*. 2012.